Editors' Suggestion

Superfluid Fraction of a 2D Bose-Einstein Condensate in a Triangular Lattice

F. Rabec,[1] G. Brochier,[1] S. Wattellier,[1] G. Chauveau,[1] Y. Li,[1] S. Nascimbene,[1] J. Dalibard,[1] and J. Beugnon[1,2,*]

[1]*Laboratoire Kastler Brossel, Collège de France, CNRS, ENS-PSL University, Sorbonne Université, 11 Place Marcelin Berthelot, 75005 Paris, France*

[2]*Institut Universitaire de France (IUF), Paris, France*

(Received 10 November 2025; accepted 27 February 2026; published 30 March 2026)

We experimentally investigate the superfluid properties of a two-dimensional, weakly interacting Bose-Einstein condensate in the zero-temperature regime when it is subjected to a triangular optical lattice potential. We implement an original method, which involves solving the hydrodynamic continuity equation to extract the superfluid fraction tensor from the measured *in situ* density distribution of the fluid at rest. In parallel, we apply an independent dynamical approach that combines compressibility and sound velocity measurements to determine the superfluid fraction. Both methods yield consistent results in good agreement with simulations of the Gross-Pitaevskii equation as well as with the Leggett bounds determined from the measured density profiles.

DOI: 10.1103/g494-rj5k

Introduction—Superfluid states of matter have been studied in many different settings, including liquid helium, atomic gases, and photonic systems [1–7]. They are usually characterized by their response to a mobile external perturbation, such as the motion of the container holding them [8]. This response can be decomposed into normal and superfluid contributions. The weight of the superfluid component is defined as the superfluid fraction f_s, a quantity that was first introduced in the context of finite-temperature systems [9]. It has been measured in liquid helium (e.g., in Refs. [10,11]) and, more recently, in atomic gases [12–15], by studying the propagation of second sound.

At zero temperature, Galilean-invariant superfluids exhibit a superfluid fraction of unity, whereas in spatially modulated systems, the superfluid fraction is reduced. Density modulations can be imposed by an external potential or occur spontaneously, as in supersolids. Determining f_s in these systems has attracted increasing interest since the realization of supersolid states in atomic gases [16–20] and polariton condensates [21]. Recent experiments have reported the measurement of f_s in a 2D Bose gas modulated along one direction [22,23], in a 1D supersolid [24,25], in a molecular BEC [26], and in a driven superfluid [27]. The superfluid fraction of zero-temperature disordered Bose gases [28,29], strongly interacting Fermi gases [30], and neutron stars [31–33] has also been studied theoretically.

In a two-dimensional modulated system, superfluidity is characterized by a superfluid tensor. It is defined from the average momentum $\langle \hat{\boldsymbol{P}} \rangle$ of a system subjected to the perturbation $-\boldsymbol{v}_0 \cdot \hat{\boldsymbol{P}}$, corresponding to the motion of an external potential with velocity $\boldsymbol{v}_0$:

$$f_s^{(i,j)} = \delta_{ij} - \lim_{\boldsymbol{v}_0 \to 0} \frac{\langle \hat{P}_j \rangle}{NM v_{0,i}}, \tag{1}$$

where N is the number of particles, M is the atomic mass, and the indices i, j are associated with the Cartesian coordinates [28,29,34]. In the experiments reported in Refs. [22,23], which studied a 2D gas modulated along the x direction, this tensor is diagonal in the (x, y) basis, $f_s^{(y,y)} = 1$, and $f_s^{(x,x)}$ is called the superfluid fraction. In these works, the superfluid fraction has been determined using various methods based on the measurement of the speed of sound, the study of scissor modes, and the calculation of the Leggett bounds from the density profile [35,36]. Such methods are well suited to 1D modulation or to cases where the density profile is a separable function of x and y. However, these methods are not generally applicable to a 2D modulation. Therefore, measuring the superfluid tensor in 2D modulated systems remains an open problem, particularly in light of the recent realization of 2D supersolids [37].

In this Letter, we apply a triangular lattice potential to a 2D, low-temperature, weakly interacting Bose condensed gas, and we study its superfluid fraction as a function of the lattice amplitude. We first introduce the Leggett bounds and compute them from the density profile of the modulated system at rest. We then describe a method, first introduced by Saslow [38], that is based on solving the continuity equation for the fluid to determine the superfluid fraction tensor solely from the density profile. Finally, we present a method based on a dynamic measurement that combines

*Contact author: beugnon@lkb.ens.fr

the determination of the cloud compressibility and the speed of sound in order to compute the superfluid fraction. These two approaches yield consistent results, and we provide a quantitative comparison with numerical simulations of the Gross-Pitaevskii equation (GPE), which accurately describes our weakly interacting BEC.

Experimental system—The experimental platform has already been described in Refs. [22,39–41]. In brief, we first produce a ^{87}Rb BEC in the magnetic sensitive hyperfine state $|F = 1, m_F = -1\rangle$ of the electronic ground level. A quasi-2D Bose gas is then obtained by loading the cloud into a single node of a vertical optical lattice. This lattice provides a strong harmonic confinement along the vertical direction z with a frequency of $\omega_z/2\pi = 4.1(2)$ kHz. The associated size of the ground-state wave function is $\ell_z = \sqrt{\hbar/M\omega_z} = 168(4)$ nm. Introducing the s-wave scattering length a_s, we obtain the 2D coupling constant $\tilde{g} = Mg/\hbar^2 = \sqrt{8\pi}a_s/\ell_z = 0.158(4)$ [42]. An additional potential generated using a digital micromirror device (DMD) creates a flat-bottom trap that confines our atoms to a square box of size $L = 42(1)$ μm. The average 2D density is fixed to $\rho_0 = 51(2)$ μm^{-2}, which corresponds to $g\rho_0/k_B = 45(2)$ nK. The temperature of the sample is below the lowest measurable value in our experiment, i.e., <20 nK, and the behavior of the gas is well approximated by the zero-temperature limit. We spatially modulate the density of the cloud in the xy plane using an optical lattice generated using a second DMD. All trapping beams consist of blue-detuned repulsive light at wavelength $\lambda = 532$ nm. The potential profile corresponds to a triangular lattice modulation given by

$$V(\boldsymbol{r}) = \bar{V} - A_L \sum_{m=0}^{2} \cos(\boldsymbol{k}_m \cdot \boldsymbol{r} + \phi_m) \tag{2}$$

with $\boldsymbol{k}_m = 4\pi/(\sqrt{3}d)\{\cos(2m\pi/3), \sin(2m\pi/3)\}$, $\boldsymbol{r} = (x, y)$, $d = 6.0(1)$ μm the lattice period, A_L the amplitude of each standing wave, and a global constant offset potential $\bar{V}$, which we set here such that $\min_{\boldsymbol{r}} V(\boldsymbol{r}) = 0$. This potential has a threefold symmetry. The global phase $\Phi = \phi_0 + \phi_1 + \phi_2$ characterizes the potential $V(\boldsymbol{r})$ of the unit cell of the lattice, whereas a variation of the ϕ_i's at constant Φ corresponds to a mere translation of the modulation pattern [43]. The lattice studied in this Letter is approximately seven periods long and corresponds to $\Phi = 0.21(1)\,\pi$. For this value of Φ, the energy of the maxima and the saddle points separating two neighboring minima are $V_0 \simeq 5.0A_L$ and $V_{\text{saddle}} \simeq 3.7A_L$, respectively. For all the lattice depths studied in this Letter, the gas remains fully connected when described in the Thomas-Fermi approximation, i.e., V_{saddle} is below the chemical potential μ_{TF} [44].

An example of the obtained density distribution is shown in Fig. 1. The projected potential is nonseparable, but due to its threefold symmetry, the superfluid tensor is expected to be isotropic (see End Matter). In the following, we thus restrict ourselves to measuring the superfluid fraction $f_s = f_s^{(y,y)} = f_s^{(x,x)}$ with $f_s^{(x,y)} = 0$.

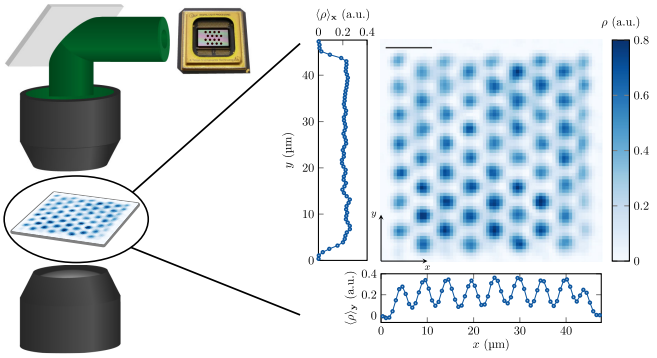

FIG. 1. Sketch of the experiment and density distribution. A triangular lattice potential is projected onto a 2D Bose-Einstein condensate using a spatial light modulator and repulsive light. High-resolution imaging is used to determine the atomic density distribution. The enlarged picture is an absorption image, averaged 40 times, of the atomic cloud subjected to a lattice potential with a depth $V_0 \simeq 4.7g\rho_0$. The color bar encodes the surface density. The length of the scale bar is 10 μm. Integrated density profiles along the x and y directions are also shown.

Analysis of the density profiles—Our study of the superfluid fraction requires an accurate determination of the *in situ* density profile of the cloud. We use here absorption imaging. Due to the finite resolution of our imaging system, the measured density $\rho^{(\text{meas})}(\boldsymbol{r})$ does not coincide with the actual density $\rho(\boldsymbol{r})$. We decompose the atomic density profile as $\rho(\boldsymbol{r}) = \rho_0 + \sum_{n>0} \rho_n(\boldsymbol{r})$, where the index n is associated with the Fourier components corresponding to a given λ_n. We have $\lambda_1 = d = 6$ μm, $\lambda_2 = d/\sqrt{3} \simeq 3.46$ μm, etc. The imaging system acts as a low-pass filter, and we describe its contribution by a set of attenuation factors $\{\beta_n\}_{n\in\mathbb{N}^*}$, which we calibrate independently up to $n = 2$ (see Ref. [44]). The measured density thus reads $\rho^{\text{meas}}(\boldsymbol{r}) = \rho_0 + \sum_{n>0} \beta_n \rho_n(\boldsymbol{r})$. For the range of density modulation explored here, we find numerically that only the first two terms, of period λ_1 and λ_2, lead to a significant contribution. We fit the experimental data to this model for the first two terms of the sum, and then we reconstruct the actual density profile $\rho(\boldsymbol{r})$ of the cloud. The fitting function is given in Ref. [44] and is chosen to ensure the isotropy of the superfluid tensor.

Leggett bounds from the density profiles—In his seminal works on supersolids, Leggett introduced two quantities f_s^+ [35] and f_s^- [36], which can be directly computed from the density profile and which provide upper and lower bounds, respectively, to the superfluid fraction of the system. These bounds have different ranges of applicability. The upper bound, based on a variational approach, is valid for any fluid with time-reversal symmetry. The applicability range

of the lower bound is more subtle. A sufficient condition is to apply it to a zero-temperature system for which a mean-field approach is valid, as is approximately the case for the weakly interacting BEC studied here. For a gas modulated along a single direction, these bounds both coincide with the superfluid fraction, a property used in Ref. [22]. For a 2D modulation, we use

$$f_s^-(\boldsymbol{e}_1) = \frac{1}{\rho_0}\left\langle \frac{1}{\left\langle \frac{1}{\rho(\boldsymbol{r})}\right\rangle_{\boldsymbol{e}_1}}\right\rangle_{\boldsymbol{e}_2} \quad \text{and} \quad f_s^+(\boldsymbol{e}_1) = \frac{1}{\rho_0}\frac{1}{\left\langle \frac{1}{\langle \rho(\boldsymbol{r})\rangle_{\boldsymbol{e}_2}}\right\rangle_{\boldsymbol{e}_1}}, \tag{3}$$

where $\langle\cdot\rangle_{\boldsymbol{e}_i}$ denotes the spatial average along direction $\boldsymbol{e}_i$, and the two directions $\boldsymbol{e}_1$ and $\boldsymbol{e}_2$ are taken to be orthogonal. For the two-dimensional system studied in this Letter, these bounds depend on the choice of the orientation of $\boldsymbol{e}_1(\theta) = \cos\theta\boldsymbol{e}_x + \sin\theta\boldsymbol{e}_y$, even in the case of the triangular lattice considered here, for which the superfluid tensor is a scalar [34]. We report in Fig. 2(a) the tightest bounds determined from the measured density profiles, which, given the chosen orientation of the studied lattice (see Fig. 1), are obtained for $f_s^-(\boldsymbol{e}_y)$ (i.e., $\theta = \pi/2$) and $f_s^+(\boldsymbol{e}_x)$ (i.e., $\theta = 0$) [46]. The colored regions in Fig. 2(a) represent the values of the superfluid fraction that are excluded by these bounds. More precisely, the lighter-colored region is permitted within the 1-σ experimental errors, while the darker regions are excluded beyond them. The superfluid fraction predicted by the GPE is shown as a solid line and mostly lies in the white and lighter-colored regions, as expected. We also illustrate in Fig. 2(b) the angular dependence of Leggett bounds computed from the density profiles for $V_0 \simeq 4.0 g\rho_0$ [34]. This confirms that the angles we have chosen to determine the tightest bounds give the highest value of the lower bound and the lowest value of the upper bound (see Ref. [44] for a comparison of the measured bounds to the GPE prediction).

Superfluid fraction from the density profile—We now turn to the determination of the superfluid fraction of the fluid directly from the measured density distribution [34,38,47]. We introduce the static equilibrium many-body wave function $\psi_{\rm eq}(\boldsymbol{r}) = \sqrt{\rho_{\rm eq}(\boldsymbol{r})}$ of the gas in the presence of the lattice potential. The superfluid fraction is associated with the modification of this wave function when switching to a reference frame moving at velocity $\boldsymbol{v}_0$. As the flow in this frame is time independent, the continuity equation reads

$$\boldsymbol{\nabla}\cdot\{\rho(\boldsymbol{r})[\boldsymbol{v}(\boldsymbol{r}) - \boldsymbol{v}_0]\} = 0, \tag{4}$$

where the velocity field is associated with the phase profile, $S(\boldsymbol{r})$, of the wave function via $\boldsymbol{v}(\boldsymbol{r}) = (\hbar/M)\boldsymbol{\nabla}S(\boldsymbol{r})$. At first order in Eq. (4), one can replace $\rho(\boldsymbol{r})$ by $\rho_{\rm eq}(\boldsymbol{r})$ and write the wave function as $e^{iS(\boldsymbol{r})}\sqrt{\rho_{\rm eq}(\boldsymbol{r})}$. The numerical resolution

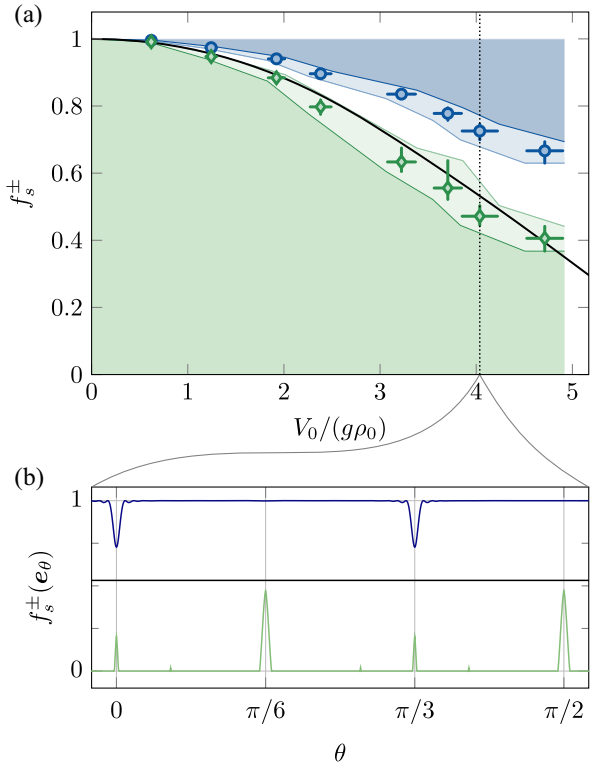

FIG. 2. Leggett bounds. (a) Measured upper bound $f_s^+(\boldsymbol{e}_x)$ (blue circles) and lower bound $f_s^-(\boldsymbol{e}_y)$ (green diamonds). Error bars correspond to the error propagation of the 1-σ uncertainties in the calibration of the imaging system response. The black solid line is the predicted superfluid fraction assuming a pure BEC described by the GPE. The colored regions define the excluded regions for the superfluid fraction according to Leggett bounds measurements. The darker-colored regions correspond to an exclusion beyond experimental errors. The white region shows the corresponding allowed region. The lighter-colored regions correspond to the intermediate region defined by the extension of experimental errors. (b) Experimentally determined upper $f_s^+(\boldsymbol{e}_1)$ (solid dark blue) and lower $f_s^-(\boldsymbol{e}_1)$ (solid light green) Leggett bounds as a function of θ, the angle between unit vector $\boldsymbol{e}_1$ and $\boldsymbol{e}_x$ for $V_0 \simeq 4.0 g\rho_0$. It can be shown that Leggett's bounds are $\pi/3$-periodic under rotation around one of the potential minima. Accordingly, the tightest bounds are achieved in (b) at $\theta = \pi/6$ or $\pi/2$ for f_s^- and at $\theta = 0$ or $\pi/3$ for f_s^+. The solid black line gives the value of f_s already shown in (a) for this lattice depth.

of this continuity equation (see End Matter), with periodic boundary conditions, yields a single solution for the phase profile $S(\boldsymbol{r})$. Using Eq. (1), one obtains the superfluid fraction tensor

$$f_s^{(i,j)} = \delta_{ij} - \lim_{\boldsymbol{v}_0\to 0}\frac{\hbar}{NMv_{0,i}}\int \mathrm{d}^2 r\, \rho_{\rm eq}(\boldsymbol{r})[\partial_j S(\boldsymbol{r})]. \tag{5}$$

We apply this approach to our experimental data to determine the superfluid fraction tensor. We show in Fig. 3 (diamonds) $f_s^{(y,y)} \equiv f_s$, which is in good agreement

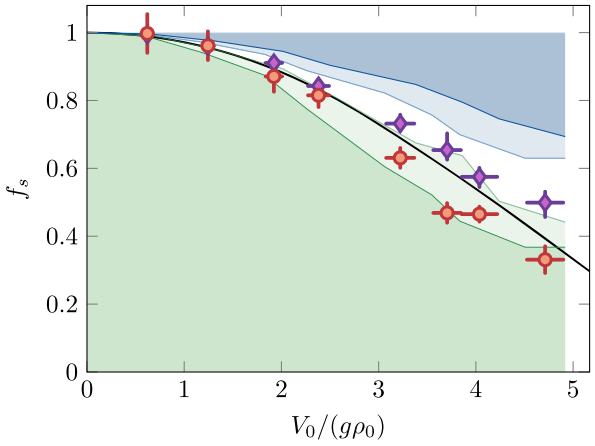

FIG. 3. Superfluid fraction measurement. Measured superfluid fraction as a function of the normalized lattice amplitude using the method based on the density profile (violet diamonds) and the dynamic approach (red circles). Error bars for the density profile methods are determined as in Fig. 2. Error bars for the dynamic approach are deduced from the sound velocity and compressibility measurements. The solid line (same as in Fig. 2) is the predicted f_s. The shaded regions represent the excluded areas for the superfluid fraction according to the Leggett bounds measurements reported in Fig. 2.

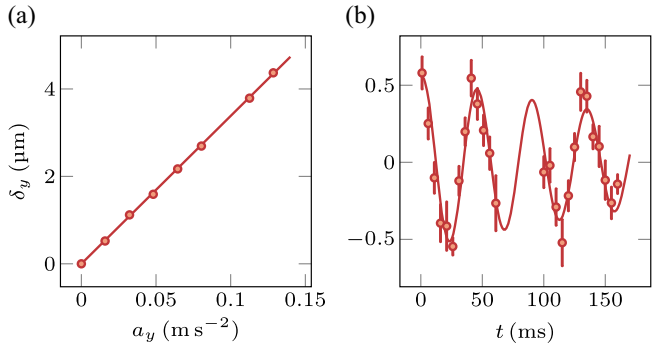

FIG. 4. Compressibility and speed of sound measurements. (a) Compressibility determined by measuring the displacement δ_y of the cloud c.m. as a function of the applied static force Ma_y to the cloud. The solid line is a fit to the data, giving a slope of $\delta_y/a_y = 34.0(7)\times10^{-6}$ s^2. From this slope, the compressibility of the cloud is found using Eq. (7). (b) Speed of sound determined from the oscillation of the c.m., δ_y, after an abrupt release of a static force. The oscillation data are fitted to an exponentially damped sine, yielding an oscillation frequency $\nu_y = 22.4(2)$ Hz. In both figures, $V_0 \simeq 2.4g\rho_0$. Injecting the measured slope and oscillation frequency in Eq. (8), we find $f_s^{(y,y)} = 0.82(2)$.

with the predicted one. In addition, it should be noted that this determination of the superfluid fraction tensor is not independent of the determination of the Leggett bounds. By construction, for each experimental density profile, the superfluid fraction lies between the two Leggett bounds. Conversely, the dynamic measurements are fully independent, and this constraint does not apply. We also performed an alternative analysis of the density profiles, allowing all Fourier components to vary freely instead of constraining f_s to be a scalar. For all lattice depths, we found the superfluid fraction tensor to be nearly isotropic, with $(f_s^{(x,x)} - f_s^{(y,y)})/f_s^{(x,x)}$ and $f_s^{(x,y)}/f_s^{(x,x)}$ typically both below 5%.

Superfluid fraction: Dynamic approach—We now describe the determination of the superfluid fraction using an independent transport measurement. In the hydrodynamic regime, in the basis where the superfluid fraction is diagonal, its coefficients are given by [9,48–50]

$$f_s^{(i,i)} = \kappa M c_i^2, \tag{6}$$

where $\kappa = (\rho_0 \partial_{\rho_0}\mu)^{-1}$ is the compressibility, a scalar quantity, and c_i is the speed of sound propagating along eigenaxis i. In the absence of the lattice, the compressibility is $\kappa_0 = 1/g\rho_0$ and the speed of sound $c_0 = \sqrt{g\rho_0/M} = 2.07(5)$ mm/s, yielding $f_s = 1$, as expected for a Galilean-invariant superfluid at $T = 0$. The approach used in previous works for 1D modulation [22,23], which relies on taking the ratio of speeds of sound to compute f_s, is not applicable to 2D modulations. Therefore, it is necessary to measure the compressibility directly in order to determine the superfluid fraction.

We measure the compressibility by applying a small constant and uniform force $F_y = Ma_y$ along direction y and by extracting the associated center-of-mass (c.m.) displacement δ_y from *in situ* absorption imaging [51]. By combining a local density approximation with a coarse graining over the lattice period, the compressibility is given by [44]

$$\kappa = \frac{12\delta_y}{F_y L^2}. \tag{7}$$

Here, the force F_y is produced by applying a static magnetic gradient so that a_y ranges from 0 to 0.13 m s^{-2}. The gradient is calibrated by *in situ* Ramsey spectroscopy [52]. An example of the measurement of δ_y as a function of a_y for $V_0 \simeq 2.4g\rho_0$ is reported in Fig. 4(a) along with a linear fit to the data. The complete set of measurements of the compressibility as a function of the lattice depth is shown in the End Matter.

We determine the speed of sound by measuring the c.m. oscillation frequency in the box potential [22]. As for the compressibility measurement, we apply a linear magnetic potential along the y direction during the preparation of the cloud, except that it is now abruptly switched off at time $t = 0$. We then measure the c.m. oscillations of the cloud and obtain its frequency, ν_y. Since we mostly excite the fundamental mode of the box, we can deduce the speed of sound from the c.m. oscillation frequency, $c_y = 2L\nu_y$. The initial applied force, corresponding to $a_y \simeq 0.019$ m/s^2, is

significantly smaller than for the compressibility measurement in order to minimize the damping of the oscillations, especially when the lattice depth is high. An example of c.m. oscillation for $V_0 \simeq 2.4 g\rho_0$ is reported in Fig. 4(b) along with a fit to the data. The complete set of speed of sound measurements for several V_0 is reported in the End Matter.

Combining the measurement of the compressibility and the speed of sound, we compute the superfluid fraction using Eq. (6), which gives

$$f_s^{(y,y)} = 48 \frac{\delta_y}{a_y} \nu_y^2, \tag{8}$$

where δ_y is measured when a static force Ma_y is applied. The resulting superfluid fraction is reported in Fig. 3 (circles) and is in excellent agreement with the one determined using the previous approach for low lattice depths. Small deviations are observed at large lattice depths. They may be linked to the observed damping of sound waves in this range of parameters (see End Matter), possibly originating from finite temperature effects, the study of which is beyond the scope of this Letter. Both determinations of f_s also lie, within experimental errors, in the region allowed by the measured Leggett bounds.

Conclusion and perspectives—Our Letter demonstrates the implementation of two methods for determining the superfluid fraction tensor in a 2D modulated weakly interacting Bose gas. These methods, based on either a dynamic approach or on the direct analysis of the *in situ* density profile of the cloud, are in good agreement with each other in our experiment. Our approach is not restricted to determining scalar superfluid fractions and can easily be extended to arbitrary lattice potentials. Dipolar supersolids are also good candidates for applying these methods, for which an approximate mean-field description is available, and their hydrodynamics is well known [34,50]. In addition, the method based on the density profile measurements, which is exact for mean-field systems, generally provides an upper bound. It can thus be used to characterize strongly interacting Fermi gases, for example, and this bound is tighter than Leggett's, as discussed for helium supersolids [53].

Acknowledgments—We thank Sandro Stringari, Kevin Geier, and Thierry Giamarchi for fruitful discussions, Sarah Philips for her participation at the final stage of this project, and Jonathan Menssen for critical reading of the manuscript. We acknowledge the support by ERC (Grant Agreement No. 863880) and by ANR (No. ANR-23-PETQ-0002).

Data availability—The data that support the findings of this article are not publicly available. The data are available from the authors upon reasonable request.

[1] P. Kapitza, Viscosity of liquid helium below the λ-point, Nature (London) **141**, 74 (1938).
[2] J. F. Allen and A. D. Misener, Flow of liquid helium II, Nature (London) **141**, 75 (1938).
[3] G. Baym, C. Pethick, and D. Pines, Superfluidity in neutron stars, Nature (London) **224**, 673 (1969).
[4] C. Raman, M. Köhl, R. Onofrio, D. S. Durfee, C. E. Kuklewicz, Z. Hadzibabic, and W. Ketterle, Evidence for a critical velocity in a Bose-Einstein condensed gas, Phys. Rev. Lett. **83**, 2502 (1999).
[5] M. W. Zwierlein, J. R. Abo-Shaeer, A. Schirotzek, C. H. Schunck, and W. Ketterle, Vortices and superfluidity in a strongly interacting Fermi gas, Nature (London) **435**, 1047 (2005).
[6] A. Amo, J. Lefrère, S. Pigeon, C. Adrados, C. Ciuti, I. Carusotto, R. Houdré, E. Giacobino, and A. Bramati, Superfluidity of polaritons in semiconductor microcavities, Nat. Phys. **5**, 805 (2009).
[7] Q. Fontaine, P.-E. Larré, G. Lerario, T. Bienaimé, S. Pigeon, D. Faccio, I. Carusotto, E. Giacobino, A. Bramati, and Q. Glorieux, Interferences between Bogoliubov excitations in superfluids of light, Phys. Rev. Res. **2**, 043297 (2020).
[8] A. J. Leggett, Superfluidity, Rev. Mod. Phys. **71**, S318 (1999).
[9] L. P. Pitaevskiĭ and S. Stringari, *Bose-Einstein Condensation and Superfluidity*, 1st ed., International Series of Monographs on Physics No. 164 (Oxford University Press, Oxford, United Kingdom, 2016).
[10] D. S. Greywall and G. Ahlers, Second-sound velocity and superfluid density in ^{4}He under pressure near T_λ, Phys. Rev. A **7**, 2145 (1973).
[11] J. Maynard, Determination of the thermodynamics of He II from sound-velocity data, Phys. Rev. B **14**, 3868 (1976).
[12] L. A. Sidorenkov, M. K. Tey, R. Grimm, Y.-H. Hou, L. Pitaevskii, and S. Stringari, Second sound and the superfluid fraction in a Fermi gas with resonant interactions, Nature (London) **498**, 78 (2013).
[13] P. Christodoulou, M. Gałka, N. Dogra, R. Lopes, J. Schmitt, and Z. Hadzibabic, Observation of first and second sound in a Berezinskii-Kosterlitz-Thouless superfluid, Nature (London) **594**, 191 (2021).
[14] T. A. Hilker, L. H. Dogra, C. Eigen, J. A. P. Glidden, R. P. Smith, and Z. Hadzibabic, First and second sound in a compressible 3D bose fluid, Phys. Rev. Lett. **128**, 223601 (2022).
[15] Z. Yan, P. B. Patel, B. Mukherjee, C. J. Vale, R. J. Fletcher, and M. W. Zwierlein, Thermography of the superfluid transition in a strongly interacting Fermi gas, Science **383**, 629 (2024).
[16] J.-R. Li, J. Lee, W. Huang, S. Burchesky, B. Shteynas, F. Ç. Top, A. O. Jamison, and W. Ketterle, A stripe phase with supersolid properties in spin–orbit-coupled Bose–Einstein condensates, Nature (London) **543**, 91 (2017).
[17] J. Léonard, A. Morales, P. Zupancic, T. Donner, and T. Esslinger, Monitoring and manipulating Higgs and Goldstone modes in a supersolid quantum gas, Science **358**, 1415 (2017).
[18] F. Böttcher, J.-N. Schmidt, M. Wenzel, J. Hertkorn, M. Guo, T. Langen, and T. Pfau, Transient supersolid properties in an

array of dipolar quantum droplets, Phys. Rev. X **9**, 011051 (2019).
[19] L. Chomaz, D. Petter, P. Ilzhöfer, G. Natale, A. Trautmann, C. Politi, G. Durastante, R. M. W. van Bijnen, A. Patscheider, M. Sohmen, M. J. Mark, and F. Ferlaino, Long-lived and transient supersolid behaviors in dipolar quantum gases, Phys. Rev. X **9**, 021012 (2019).
[20] L. Tanzi, E. Lucioni, F. Famà, J. Catani, A. Fioretti, C. Gabbanini, R. N. Bisset, L. Santos, and G. Modugno, Observation of a dipolar quantum gas with metastable supersolid properties, Phys. Rev. Lett. **122**, 130405 (2019).
[21] D. Trypogeorgos, A. Gianfrate, M. Landini, D. Nigro, D. Gerace, I. Carusotto, F. Riminucci, K. W. Baldwin, L. N. Pfeiffer, G. I. Martone *et al.*, Emerging supersolidity in photonic-crystal polariton condensates, Nature (London) **639**, 337 (2025).
[22] G. Chauveau, C. Maury, F. Rabec, C. Heintze, G. Brochier, S. Nascimbene, J. Dalibard, J. Beugnon, S. M. Roccuzzo, and S. Stringari, Superfluid fraction in an interacting spatially modulated Bose-Einstein condensate, Phys. Rev. Lett. **130**, 226003 (2023).
[23] J. Tao, M. Zhao, and I. B. Spielman, Observation of anisotropic superfluid density in an artificial crystal, Phys. Rev. Lett. **131**, 163401 (2023).
[24] L. Tanzi, J. G. Maloberti, G. Biagioni, A. Fioretti, C. Gabbanini, and G. Modugno, Evidence of superfluidity in a dipolar supersolid from nonclassical rotational inertia, Science **371**, 1162 (2021).
[25] G. Biagioni, N. Antolini, B. Donelli, L. Pezzè, A. Smerzi, M. Fattori, A. Fioretti, C. Gabbanini, M. Inguscio, L. Tanzi, and G. Modugno, Measurement of the superfluid fraction of a supersolid by Josephson effect, Nature (London) **629**, 773 (2024).
[26] L. Pezzè, K. Xhani, C. Daix, N. Grani, B. Donelli, F. Scazza, D. Hernandez-Rajkov, W. J. Kwon, G. Del Pace, and G. Roati, Stabilizing persistent currents in an atomtronic Josephson junction necklace, Nat. Commun. **15**, 4831 (2024).
[27] N. Liebster, M. Sparn, E. Kath, J. Duchene, H. Strobel, and M. K. Oberthaler, Supersolid-like sound modes in a driven quantum gas, Nat. Phys. **21**, 1064 (2025).
[28] K. T. Geier, J. Maki, A. Biella, F. Dalfovo, S. Giorgini, and S. Stringari, Superfluidity and sound propagation in disordered Bose gases, Phys. Rev. Res. **7**, 013187 (2025).
[29] D. Pérez-Cruz, G. E. Astrakharchik, and P. Massignan, Superfluid fraction of interacting bosonic gases, Phys. Rev. A **111**, L011302 (2025).
[30] G. Orso and S. Stringari, Superfluid fraction and Leggett bound in a density-modulated strongly interacting Fermi gas at zero temperature, Phys. Rev. A **109**, 023301 (2024).
[31] N. Chamel, Superfluid fraction in the crystalline crust of a neutron star: Role of BCS pairing, Phys. Rev. C **111**, 045803 (2025).
[32] G. Almirante and M. Urban, Superfluid fraction in the slab phase of the inner crust of neutron stars, Phys. Rev. C **109**, 045805 (2024).
[33] G. Almirante and M. Urban, Superfluid density in linear response theory: Pulsar glitches from the inner crust of neutron stars, Phys. Rev. Lett. **135**, 132701 (2025).
[34] P. B. Blakie, Superfluid fraction tensor of a two-dimensional supersolid, J. Phys. B **57**, 115301 (2024).
[35] A. J. Leggett, Can a solid be "superfluid"?, Phys. Rev. Lett. **25**, 1543 (1970).
[36] A. J. Leggett, On the superfluid fraction of an arbitrary many-body system at $T = 0$, J. Stat. Phys. **93**, 927 (1998).
[37] M. A. Norcia, C. Politi, L. Klaus, E. Poli, M. Sohmen, M. J. Mark, R. N. Bisset, L. Santos, and F. Ferlaino, Two-dimensional supersolidity in a dipolar quantum gas, Nature (London) **596**, 357 (2021).
[38] W. M. Saslow, Superfluidity of periodic solids, Phys. Rev. Lett. **36**, 1151 (1976).
[39] J. L. Ville, T. Bienaimé, R. Saint-Jalm, L. Corman, M. Aidelsburger, L. Chomaz, K. Kleinlein, D. Perconte, S. Nascimbène, J. Dalibard, and J. Beugnon, Loading and compression of a single two-dimensional Bose gas in an optical accordion, Phys. Rev. A **95**, 013632 (2017).
[40] J. L. Ville, R. Saint-Jalm, É. Le Cerf, M. Aidelsburger, S. Nascimbène, J. Dalibard, and J. Beugnon, Sound propagation in a uniform superfluid two-dimensional Bose gas, Phys. Rev. Lett. **121**, 145301 (2018).
[41] Y.-Q. Zou, É. L. Cerf, B. Bakkali-Hassani, C. Maury, G. Chauveau, P. C. M. Castilho, R. Saint-Jalm, S. Nascimbene, J. Dalibard, and J. Beugnon, Optical control of the density and spin spatial profiles of a planar Bose gas, J. Phys. B **54**, 08LT01 (2021).
[42] I. Bloch, J. Dalibard, and W. Zwerger, Many-body physics with ultracold gases, Rev. Mod. Phys. **80**, 885 (2008).
[43] The case $\Phi = 0$ corresponds to the so-called "triangular" lattice potential (associated with the hexagonal lattice in Bravais classification), which has sixfold symmetry, and the case $\Phi = \pi$ to the honeycomb lattice potential.
[44] See Supplemental Material at http://link.aps.org/supplemental/10.1103/g494-rj5k for details on the optical potential, Leggett bounds, and the determination of the compressibility, which includes Ref. [45].
[45] C. Dorrer and J. D. Zuegel, Design and analysis of binary beam shapers using error diffusion, J. Opt. Soc. Am. B **24**, 1268 (2007).
[46] This is also the case for a triangular lattice with $\Phi = 0$.
[47] N. Sepúlveda, C. Josserand, and S. Rica, Superfluid density in a two-dimensional model of supersolid, Eur. Phys. J. B **78**, 439 (2010).
[48] J. Hofmann and W. Zwerger, Hydrodynamics of a superfluid smectic, J. Stat. Mech. (2021) P033104.
[49] L. M. Platt, D. Baillie, and P. B. Blakie, Sound waves and fluctuations in one-dimensional supersolids, Phys. Rev. A **110**, 023320 (2024).
[50] E. Poli, D. Baillie, F. Ferlaino, and P. B. Blakie, Excitations of a two-dimensional supersolid, Phys. Rev. A **110**, 053301 (2024).
[51] E. Busley, L. E. Miranda, A. Redmann, C. Kurtscheid, K. Umesh, F. Vewinger, M. Weitz, and J. Schmitt, Compressibility and the equation of state of an optical quantum gas in a box, Science **375**, 1403 (2022).
[52] F. Rabec, G. Chauveau, G. Brochier, S. Nascimbene, J. Dalibard, and J. Beugnon, Bloch oscillations of a soliton

in a one-dimensional quantum fluid, Nat. Phys. **21**, 1541 (2025).
[53] W. M. Saslow, On the superfluid fraction and the hydrodynamics of supersolids, J. Low Temp. Phys. **169**, 248 (2012).
[54] C. Josserand, Y. Pomeau, and S. Rica, Patterns and supersolids, Eur. Phys. J. Spec. Top. **146**, 47 (2007).
[55] C. Josserand, Y. Pomeau, and S. Rica, Coexistence of ordinary elasticity and superfluidity in a model of a defect-free supersolid, Phys. Rev. Lett. **98**, 195301 (2007).
[56] N. Sepúlveda, C. Josserand, and S. Rica, Nonclassical rotational inertia fraction in a one-dimensional model of a supersolid, Phys. Rev. B **77**, 054513 (2008).

End Matter

Appendix A: Compressibility measurement—We show in Fig. 5 the measured compressibility normalized to the compressibility κ_0 of a uniform system. We obtain an excellent agreement with the GPE prediction.

Appendix B: Measurement of the c.m. oscillation frequency—To extract the oscillation frequency of the cloud confined in the box potential after an excitation along the y direction, we model the time evolution of the c.m. of the cloud as a damped free harmonic oscillator [22,40],

$$\ddot{\delta}_y + \Gamma_y \dot{\delta}_y + \omega_y^2 \delta_y = 0, \tag{B1}$$

whose solution for zero initial velocity is

$$\delta_y(t) = \delta_{y,0} + A e^{-\Gamma_y t/2}\left[\cos(\Omega_y t) + \frac{\Gamma_y}{2\Omega_y}\sin(\Omega_y t)\right], \tag{B2}$$

where $\Omega_y = \sqrt{\omega_y^2 - \Gamma_y^2/4}$ and assuming $\Gamma_y < 2\omega_y$. We fit our data to this model with $\delta_{y,0}$, Γ_y, A, and ω_y as fit parameters. The oscillator frequency $\omega_y = 2\pi\nu_y$ is used to compute the speed of sound and the superfluid fraction. We show in Fig. 6 the fitted values of ω_y and Γ_y for different lattice depths. Using these results, we determine the speed of sound normalized to the speed of sound in the absence of a lattice, c_0, as shown in Fig. 7. The experimental data are in good agreement with the simulation. At large lattice depths, we notice a deviation to lower values of the measured speed of sound compared with the GPE prediction. This may be due to minor deviations in the lattice potential compared to Eq. (2) or to finite-temperature effects, the study of which is beyond the scope of this Letter.

Appendix C: Upper bounds for the superfluid fraction—We detail here the derivation of the method used in the main text to compute the superfluid fraction for systems at zero temperature and its applicability beyond weakly interacting Bose gases.

We consider a two-dimensional system of area $L_x \times L_y$ with periodic boundary conditions and consisting of N particles. We assume the system has time-reversal symmetry and that its ground state $|\Psi_{\mathrm{eq}}\rangle$ does not break this symmetry. The wave function Ψ_{eq} can thus be chosen as real. To compute the superfluid fraction tensor, we look for the ground state with twisted boundary conditions (TBC),

$$\begin{aligned}\Psi(\cdots, \boldsymbol{r}_k + L_x \boldsymbol{e}_x, \cdots) &= \Psi(\cdots, \boldsymbol{r}_k, \cdots)\exp(-\mathrm{i}u_x L_x)\\ \Psi(\cdots, \boldsymbol{r}_k + L_y \boldsymbol{e}_y, \cdots) &= \Psi(\cdots, \boldsymbol{r}_k, \cdots)\exp(-\mathrm{i}u_y L_y)\end{aligned} \tag{C1}$$

with $u_x L_x, u_y L_y \ll 2\pi$. The superfluid fraction tensor is then given by the energy increase of the ground state at lowest order in $\boldsymbol{u} = u_x \boldsymbol{e}_x + u_y \boldsymbol{e}_y$ [35],

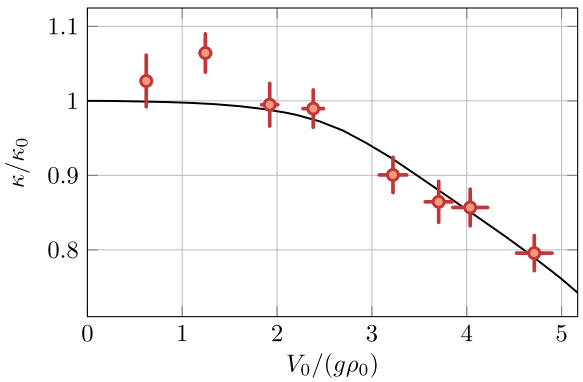

FIG. 5. Compressibility measurement. Normalized compressibility as a function of the normalized lattice amplitude. The solid line represents the corresponding prediction given by the GPE. Error bars correspond to the 1-σ statistical uncertainty, typically obtained from 40 repetitions of the experiment.

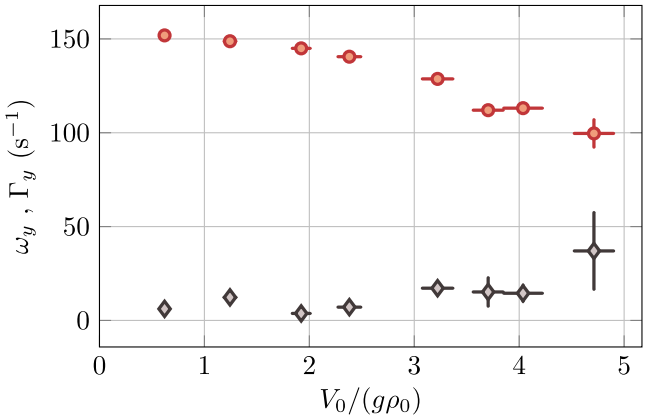

FIG. 6. Angular frequency and damping of the oscillations. Angular frequency (red circles) and damping coefficient (gray diamonds) of the c.m. oscillations used to measure the speed of sound. Error bars correspond to the 1-σ statistical uncertainty obtained from 10 repetitions of the experiment.

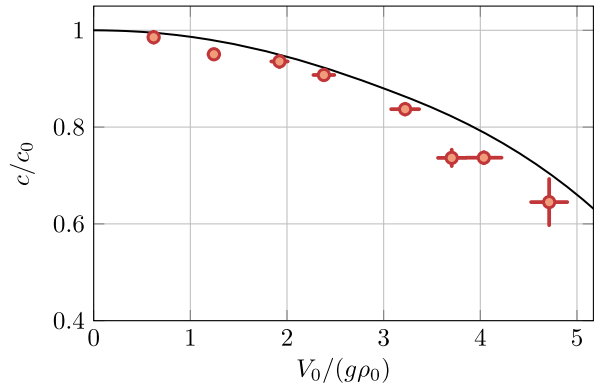

FIG. 7. Speed of sound measurement. Normalized speed of sound as a function of the normalized lattice amplitude. The solid line represents the prediction given by the GPE. Error bars correspond to the 1-σ statistical uncertainty obtained from 10 repetitions of the experiment.

$$\Delta E(\boldsymbol{u}) \equiv E(\boldsymbol{u}) - E_0 = \frac{N\hbar^2}{2M} \sum_{\alpha,\beta=x,y} f_s^{(\alpha,\beta)} u_\alpha u_\beta. \tag{C2}$$

To obtain upper bounds on the eigenvalues of the positive symmetric tensor f_s, we adopt a variational method. We take the variational ansatz,

$$\Psi_{\text{trial}}(\boldsymbol{r}_1, \ldots, \boldsymbol{r}_N) = \Psi_{\text{eq}}(\boldsymbol{r}_1, \ldots, \boldsymbol{r}_N) \exp\left(\mathrm{i} \sum_{i=1}^{N} \tilde{S}(\boldsymbol{r}_i) \right), \tag{C3}$$

where $\tilde{S}$ is chosen so that Ψ_{trial} satisfies the TBC:

$$\begin{aligned} \tilde{S}(x + L_x, y) &= \tilde{S}(x, y) - u_x L_x, \\ \tilde{S}(x, y + L_y) &= \tilde{S}(x, y) - u_y L_y. \end{aligned} \tag{C4}$$

The corresponding energy increase is then

$$\Delta E_{\text{trial}}(\boldsymbol{u}) \equiv E_{\text{trial}}(\boldsymbol{u}) - E_0 = \frac{\hbar^2}{2M} \int \rho_{\text{eq}}(\boldsymbol{r}) \left(\boldsymbol{\nabla} \tilde{S}(\boldsymbol{r})\right)^2 \mathrm{d}^2 r, \tag{C5}$$

where $\rho_{\text{eq}}(\boldsymbol{r}) = N \int \Psi_{\text{eq}}^2(\boldsymbol{r}, \boldsymbol{r}_2, \ldots, \boldsymbol{r}_N) \mathrm{d}^2 r_2 \ldots \mathrm{d}^2 r_N$ is the particle density. For any choice of $\tilde{S}$ fulfilling the TBC, $\Delta E_{\text{trial}}(\boldsymbol{u})$ gives an upper bound on $\Delta E(\boldsymbol{u})$. The tightest bound is obtained by choosing the function $\tilde{S}$ that minimizes the trial energy, which obeys

$$\boldsymbol{\nabla} \cdot \left(\rho_{\text{eq}}(\boldsymbol{r}) \boldsymbol{\nabla} \tilde{S}(\boldsymbol{r}) \right) = 0. \tag{C6}$$

This equation can be solved with the constraint given in Eq. (C4), yielding an expression for $\tilde{S}$ at first order in $\boldsymbol{u}$. The trial energy increase, Eq. (C5), is thus of order 2 in $\boldsymbol{u}$, which allows us to define the positive and symmetric rank-2 tensor g_s:

$$\Delta E_{\text{trial}}(\boldsymbol{u}) = \frac{N\hbar^2}{2M} \sum_{\alpha,\beta=x,y} g_s^{(\alpha,\beta)} u_\alpha u_\beta. \tag{C7}$$

We introduce the two eigenvalues, $f_{s,1}, f_{s,2}$ (resp. $g_{s,1}, g_{s,2}$) of the tensor f_s (resp g_s). Assuming, without loss of generality, $f_{s,1} \leq f_{s,2}$ and $g_{s,1} \leq g_{s,2}$, one can deduce from the general inequality $\Delta E(\boldsymbol{u}) \leq \Delta E_{\text{trial}}(\boldsymbol{u})$ for all $\boldsymbol{u}$ that

$$f_{s,1} \leq g_{s,1} \qquad f_{s,2} \leq g_{s,2}. \tag{C8}$$

These inequalities hold even if the eigenvectors of f_s and g_s do not coincide and are valid for any system at zero temperature with time-reversal symmetry.

It is interesting to compare this approach to Leggett's [35], which is most relevant when the eigenaxes of f_s are already known. Consider a phase twist along one of these axes, say x, so that the total current along the perpendicular axis is zero:

$$J_y = \frac{\hbar}{M} \int \rho_{\text{eq}}(\boldsymbol{r}) \partial_y \tilde{S} \, \mathrm{d}^2 r = 0. \tag{C9}$$

The approach above deals with an ansatz for $\tilde{S}$ that depends on both x and y, allowing local currents with arbitrary directions while fulfilling $J_y = 0$, whereas the Leggett approach uses a more restrictive ansatz by assuming that the phase $\tilde{S}$ depends only on x.

For systems where the ground state satisfies the right-hand side of Eq. (C3) at lowest order in $\boldsymbol{u}$ when subjected to twisted boundary conditions, the tensors f_s and g_s coincide. In the case of a weakly interacting Bose gas at zero temperature, the many-body wave function is given by a product of identical single-particle wave functions obeying the GPE. In the presence of TBC, the wave function can be written as $\sqrt{\rho_{\text{eq}}(\boldsymbol{r}) + \delta\rho(\boldsymbol{r})} e^{\mathrm{i}\tilde{S}(\boldsymbol{r})}$. The corresponding energy increase is given by the same term as in the right-hand side of Eq. (C5), $\hbar^2/(2M) \int \rho_{\text{eq}}(\boldsymbol{r}) (\boldsymbol{\nabla} \tilde{S}(\boldsymbol{r}))^2 \mathrm{d}^2 r$, and a term $\propto \int (\boldsymbol{\nabla} \delta\rho)^2$. The minimum of this second term is obtained independently of $S(\boldsymbol{r})$ and for $\delta\rho(\boldsymbol{r}) = 0$. It justifies that, in this case, g_s coincides with the superfluid fraction tensor f_s. We recover the expressions used in the main text by introducing the phase $S(\boldsymbol{r}) = \tilde{S}(\boldsymbol{r}) + \boldsymbol{u} \cdot \boldsymbol{r}$, which obeys periodic boundary conditions. Equation (C6) then reads

$$\boldsymbol{\nabla} \cdot \{ \rho_{\text{eq}}(\boldsymbol{r}) [\boldsymbol{\nabla} S(\boldsymbol{r}) - \boldsymbol{u}] \} = 0. \tag{C10}$$

Integrating by parts in Eq. (C5), we find [34,47,54–56]

$$\Delta E(\boldsymbol{u}) = \frac{N\hbar^2}{2M} \boldsymbol{u}^2 - \frac{\hbar^2}{2M} \int \rho_{\text{eq}}(\boldsymbol{r}) \boldsymbol{u} \cdot \boldsymbol{\nabla} S(\boldsymbol{r}) \, \mathrm{d}^2 r, \tag{C11}$$

from which we deduce Eq. (5).

Appendix D: Isotropy of the superfluid tensor for the triangular lattice—For the triangular lattice, the energy $\Delta E(\boldsymbol{u})$, which is a quadratic form in $\boldsymbol{u}$, is invariant under the transformations

$$u_x \to -\frac{1}{2}u_x \pm \frac{\sqrt{3}}{2}u_y \qquad u_y \to \mp\frac{\sqrt{3}}{2}u_x - \frac{1}{2}u_y. \quad \text{(D1)}$$

One immediately deduces that $f_s^{(x,x)} = f_s^{(y,y)}$ and $f_s^{(x,y)} = 0$.